Macromolecules

Cite This: Macromolecules 2019, 52, 8989−8999

Article

pubs.acs.org/Macromolecules

Experiments and Simulations Probing Local Domain Bulge and String Assembly of Aligned Nanoplates in a Lamellar Diblock Copolymer

Nadia M. Krook,[†,⊥] Christian Tabedzki,[‡,⊥] Katherine C. Elbert,[§] Kevin G. Yager,[∥] Christopher B. Murray,*[,†,§] Robert A. Riggleman,*[,‡] and Russell J. Composto*[,†]

[†]Department of Materials Science and Engineering, [‡]Department of Chemical and Biomolecular Engineering, and [§]Department of Chemistry, University of Pennsylvania, Philadelphia, Pennsylvania 19104, United States

[∥]Center for Functional Nanomaterials, Brookhaven National Lab, Upton, New York 11973, United States

Supporting Information

ABSTRACT: Within ordered poly(styrene-*b*-methyl methacrylate) (PS-*b*-PMMA) block copolymer (BCP) lamellae, oriented nanoplates [gadolinium trifluoride doped with ytterbium and erbium, GdF_3:Yb/Er (20/2 mol %)] grafted with polyethylene glycol assemble into aligned strings at small interparticle separations. Herein, we investigate the origin of these aligned assemblies using X-ray scattering, electron microscopy, and hybrid particle/self-consistent field theory simulations. From previous reports, the insertion of a nanoplate in a BCP microdomain is expected to perturb the polymer chains and produce a local domain bulge as the PS/PMMA interface distorts to optimize conformational entropy. While experimental techniques are unable to directly resolve this small distortion, the two-dimensional simulations of the equilibrium BCP nanocomposite structure clearly show bulge formation around the nanoplates. As a function of particle separation, the potential of mean force (PMF) calculation reveals a global minimum corresponding to an equilibrium interparticle spacing of 7.0 nm, which agrees well with a mean experimental value of 6.4 nm. Furthermore, the PMF calculation exhibits a small activation barrier due to the high curvature penalty between two nanoplates at a separation distance of 21.7 nm. Ultimately, nanoplate strings form to fulfill the criteria where the energy benefit of decreasing interfacial area and minimizing chain stretching outweighs the energy penalty associated with reducing the translational entropy affiliated with evenly distributing the nanoplates. The simulations also illustrate a narrow tolerance for orientation angles, supporting the high degree of nanoplate alignment observed experimentally. We anticipate that the ability to align and couple anisotropic nanoparticles in BCPs presents opportunities to create functional polymer nanocomposites with orientation-dependent properties.

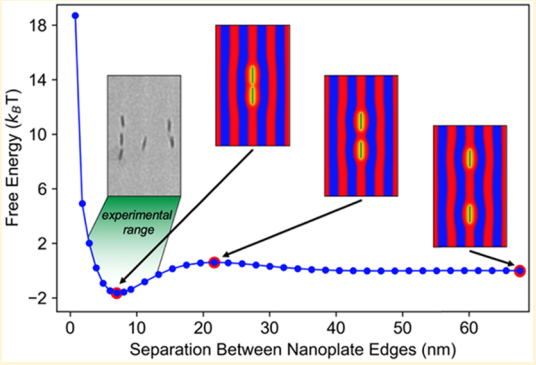

INTRODUCTION

Block copolymer (BCP)-based supramolecules[1−5] and traditional block copolymers (BCPs)[6−8] offer a nanostructured matrix to template the assembly of nanoparticles (NPs). Provided that NP and polymer compatibility (geometric and thermodynamic) has been considered, polymer nanocomposites (PNCs) can be designed with nanoscale building blocks arranged into hierarchical architectures to achieve a desired structure−property relationship. Factors including matrix molecular weight and chemical composition, brush chain length, grafting density, and chemistry as well as particle size and volume fraction, directly impact how NPs will organize within these hybrid materials. Since the publication of several pioneering studies[9−18] in both theory and experiments, significant progress has been made toward understanding how these factors affect the dispersion of spherical NPs in BCPs.

Meanwhile, fewer studies have explored the effects of particle shape anisotropy (rods[2−4,19−21] and plates[5,22]) in BCP nanocomposites. Directing the orientation of nonspherical NPs is of particular interest for exploiting their shape-dependent properties for a variety of applications[23] including photovoltaics,[24−26] metamaterials,[27,28] biomimetic systems,[29] and thermal interface materials.[30] BCPs deliver a versatile approach to creating large-area, self-assembled nanocomposites that direct anisotropic particle orientation through limited processing steps. However, unresolved questions prevent BCPs from being fully harnessed to engineer hybrid materials with precisely directed NP orientations. These questions include a fundamental understanding of how locally disrupting the equilibrium BCP microstructure, from polymer chains

Received: June 25, 2019
Revised: October 3, 2019
Published: November 13, 2019

DOI: 10.1021/acs.macromol.9b01324
Macromolecules 2019, 52, 8989−8999

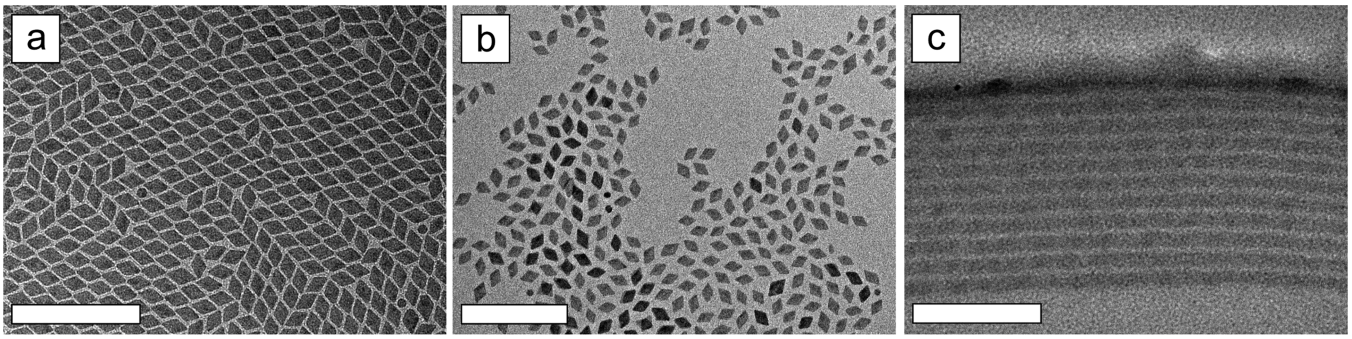

Figure 1. Representative transmission electron microscopy (TEM) (JEM-1400, 120 kV) micrographs of (a) a monolayer of as-synthesized GdF_3:Yb/Er (20/2 mol %) with OA on their surfaces, (b) drop-casted M_n = 5 kg/mol PEG-PO_3H_2-functionalized nanoplates, and (c) an ultramicrotomed cross-section of neat lamellar-forming M_n = 38k-*b*-36.8k g/mol PS-*b*-PMMA film (thickness ~370 nm) annealed at 190 °C for 48 h. The light and dark domains of the BCP are PMMA and PS, respectively. All scale bars are 200 nm.

rearranging to accommodate a nonspherical NP, might lead to interparticle assembly within a domain.

Recently, we showed that crystalline gadolinium trifluoride rhombic nanoplates doped with ytterbium and erbium [GdF_3:Yb/Er (20/2 mol %)] and functionalized with favorable interactions for one domain will align in ordered BCP lamellae at low NP volume fractions.[22] In this first study, it was observed that the aligned nanoplates further assemble and string together in chains in the confining domain at small interparticle distances. Anisotropic assemblies of polymer-grafted NPs have been previously shown in homopolymer[31−34] and BCP[2,4,5,20] matrices. However, without tuning interparticle interactions to intentionally form NP strings, we focus on the thermodynamic origins of nanoplate assemblies from our initial experiments with supporting simulations.

Bockstaller et al. predicted that, in the presence of a nanoplate, a bulge would be created in a BCP domain as a result of excessive chain perturbations.[6] However, the present work will discuss the limitations of observing this phenomenon experimentally using electron microscopy and scattering techniques. Instead, polymer field theory allows researchers to effectively study and model BCP nanocomposite physics.[9,10,35−38] Furthermore, theoretical studies have captured the anticipated domain distortion around spherical NPs.[36−38] By coupling experiments with the theory, the present work seeks to elucidate the mechanism by which GdF_3:Yb/Er nanoplates grafted with polyethylene glycol (PEG) confined in poly(styrene-*b*-methyl methacrylate) (PS-*b*-PMMA) lamellae create a bulge in the microdomain and contribute to the anisotropic assembly of these aligned particles.

The simulation results predict and a deeper experimental exploration corroborates an equilibrium interparticle spacing between GdF_3:Yb/Er NPs assembled in anisotropic strings. Here, we propose that nanoplates bridge together to mediate the following energetic penalties: the increased interfacial area between the PS and PMMA domains accompanied by the decreased chain entropy from highly stretched and compressed chains around the nanoplates. The simulations also reveal an intermediate nanoplate separation that corresponds to a local free energy maximum. This interparticle spacing relates to a separation where the excess interfacial area of two plates only begins to merge, creating a PS/PMMA interface of the highest curvature. We acknowledge that, rather than one-dimensional strings, the nanoplates may be assembling as sheets or two-dimensional (2D) arrays in the plane of the PMMA domain in the experimental system. However, since a projection of the film cross-section is captured in the microscopy images, the assemblies have the appearance of strings and will, therefore, continue to be referred to as such. We also present additional simulations as a function of nanoplate orientation. The findings from these simulations support nanoplate alignment with some tilt allowance in the experimental system by illustrating a narrow tolerance for orientation angles in the studied, low M_n, BCP. Creating aligned NP assemblies within the domain of a BCP may provide a platform to fabricate functional nanomaterials that would benefit from strategically aligning and coupling particles into anisotropic arrays.[39]

METHODS

Materials. All polymers and chemicals were used as received. Phosphoric acid-functionalized poly(ethylene glycol) (PEG-PO_3H_2, M_n = 5 kg/mol) was purchased from Nanocs Inc., and lamellar-forming poly(styrene-*b*-methyl methacrylate) (PS-*b*-PMMA, M_n = 38k-*b*-36.8k g/mol, PDI = 1.08) was purchased from Polymer Source Inc. Toluene (99.9%, for high-performance liquid chromatography (HPLC)) was purchased from Sigma-Aldrich, while hydrogen peroxide (H_2O_2, 30%, certified ACS), sodium hydroxide solution (NaOH, 50% w/w, certified), and sulfuric acid (H_2SO_4, certified ACS plus) were purchased from Fisher Scientific. Silicon (Si) wafers with a 300 nm wet thermal oxide layer were purchased from University Wafer. EpoxiCure 2 epoxy hardener and resin were both purchased from Buehler.

The synthesis of oleic acid (OA)-stabilized GdF_3:Yb/Er (20/2 mol %) rhombic nanoplates [longest diagonal (d_1) = 35 nm, shortest diagonal (d_2) = 22 nm, and thickness (t) = 3 nm] in Figure 1a and subsequent surface modification with σ = 0.62 chains/nm^2 of M_n = 5 kg/mol PEG-PO_3H_2 were previously reported.[22] The PEG-PO_3H_2-functionalized nanoplates in Figure 1b were dispersed in toluene as a stock solution until further use.

Block Copolymer Nanocomposite Preparation. Si wafers with a 300 nm wet thermal oxide layer were cut to 1 cm^2. The substrates were piranha-cleaned (70:30 vol %, H_2SO_4:H_2O_2) at 80 °C for 20 min, rinsed three times, and stored overnight in deionized (DI) H_2O before drying with N_2 followed by 10 min of UV ozone treatment. Meanwhile, the polymer-functionalized GdF_3:Yb/Er nanoplates were added to 7 wt % solutions of M_n = 38k-*b*-36.8k g/mol PS-*b*-PMMA in toluene and stirred with a magnetic stir bar for at least 2 h at 40 °C. Once the polymer was dissolved, the solutions were spin-coated (2000 rpm, 1 min) onto the cleaned Si substrates. The films were annealed under vacuum at 190 °C for 48 h. The BCP nanocomposite samples that were formed had the following final nanoplate volume fractions: ϕ = 0 (Figure 1c), ϕ = 0.0083 (Figure S1), ϕ = 0.017 (Figure S2), ϕ = 0.027, ϕ = 0.038, ϕ = 0.050, and ϕ = 0.064. A F3-

DOI: 10.1021/acs.macromol.9b01324
Macromolecules 2019, 52, 8989−8999

UV reflectometer (Filmetrics, LS-DT2 light source and SS-5 stage) was used to measure film thicknesses.

Grazing-Incidence Small-Angle X-ray Scattering (GISAXS). Experiments were performed at the Soft Matter Interfaces (12-ID) and Complex Materials Scattering (11-BM) beamlines at the National Synchrotron Light Source II (Brookhaven National Laboratory). Scattering data was collected using pixel-array detectors; conversion from the detector space to reciprocal space was calibrated by measuring a standard sample (silver behenate). We define q_z to be the vertical (film normal) direction, q_x to be the orthogonal horizontal (in-plane) direction, q_y to be the direction along the beam, and $q_r = \sqrt{q_x^2 + q_y^2}$ to be the total magnitude of the in-plane scattering component. To analyze the in-plane repeat spacing of the structures, we extracted a linecut along the q_r direction (slightly above the Yoneda[40,41]), fit the first-order peak to a Gaussian, and converted to real space using $d = 2\pi/q$. To determine the out-of-plane repeat spacing, one must account for the shift in the scattering peaks arising from refraction distortion effects.[42−44] The nominal (detector space) peak position (q_0) was determined by taking a linecut along q_z (at the q_r position of the primary peak immediately adjacent to the beamstop) and fit the scattering peak to a Gaussian. This scattering peak arises from the periodic order in the vertical (film normal) direction, due to the horizontal lamellae stacking. However, the true q_z position for this peak is shifted due to refraction of the incident and scattered X-rays, leading to a nominal peak position on the detector that must be corrected.[42] The refraction correction for a peak arising from the transmission channel (q_T) is different than for the reflection channel (q_R). For the data analysis herein, we selected the peak around 0.057 Å^{-1} on the detector, which is the third-order lamellar scattering peak. This higher-order is selected since the first and second-order peaks appear below the horizon and superimposed on the Yoneda and are, thus, strongly affected by substrate absorption and Yoneda scattering. We confirmed that this scattering peak arises from the transmission channel by varying the grazing-incidence angle and applied a refraction correction based on the known incidence angle and a calculated value for the critical angle of the film (0.098° for PMMA at 13.5 keV). Examples of typical peak analyses are shown in Figure S3.

Transmission Electron Microscopy (TEM). Films were lifted from the substrates by floating them on the surface of a NaOH solution (80:20 vol %, DI H_2O:50% w/w NaOH solution) at 40 °C. Once the films delaminated from the Si, they were rinsed in a DI H_2O bath and lifted onto Teflon. After water evaporation, the top of the BCP nanocomposite surfaces was sputter-coated with a thin layer of gold (Au) and palladium (Pd) and transferred from the Teflon into two-part epoxy. Film cross-sections (~50−70 nm thick) were cut by ultramicrotomy (Leica Ultracut S Ultramicrotome) with a diamond knife. TEM characterization of the BCP nanocomposite cross-sections deposited on carbon-coated grids was performed with a JEOL JEM-1400 TEM operated at 120 kV.

Nanoplate Separation Image Analysis. The separation between NP edges within assembled strings of aligned nanoplates was analyzed using ImageJ (v 1.52a). This process is shown in Figure S4. Briefly, TEM images of the BCP nanocomposite sample containing ϕ = 0.017 nanoplates (Figure S4a) were manually thresholded to isolate all of the nanoplate areas and converted into binary images (Figure S4b). A straight line selection was drawn along the nanoplate strings in the binary images (Figure S4b). By performing a plot profile analysis to graph the pixel intensities as a function of distance (Figure S4c), 300 edge-to-edge distances between aligned nanoplates assembled in strings were measured at half the maximum intensity value. All 300 measurements that were taken are listed in Table S1.

Description of the Simulations. To model the experimental system, hybrid particle/self-consistent field theory (hSCFT) was implemented based on the previous literature.[21,37,45−50] The model presented herein is adjusted to account for the slightly negative Flory−Huggins interaction parameter (χ) between the PMMA domain of the BCP and the PEG brushes grafted to the nanoplates, as demonstrated by Hore et al.[51] Since the model can be used for various polymeric systems, generic variables (A, B, C) are used to represent the three polymeric components. For our specific experimental system, A is PS, B is PMMA, and C is the grafted PEG.

Polymer chains are represented as discrete Gaussian chains with the statistical segment size b. Explicit NPs are modeled with cavity functions to exclude polymers from certain areas of the simulations. To represent shape anisotropy, the following functional form (Γ) for the NP, used by Rasin et al. to simulate anisotropic particles,[21] is employed

$$\Gamma(\mathbf{r}) = \frac{\rho_0}{4}\,\mathrm{erfc}\left(\frac{\left(|\mathbf{u}\cdot(\mathbf{r}-\mathbf{r}_c)| - \frac{L_P}{2}\right)}{\xi}\right)\mathrm{erfc}\left(\frac{(|\mathbf{u}\times(\mathbf{r}-\mathbf{r}_c)| - R_P)}{\xi}\right) \tag{1}$$

where R_P is the NP radius, L_P is the NP length, ρ_0 is the bulk density of the system, and ξ is the NP interface width, which controls how quickly the particle density goes from ρ_0 to 0. Within any given simulation, the NP positions $\mathbf{r}_c$ and orientations $\mathbf{u}$ are fixed. The probability distribution of grafting sites for the model PEG brushes is defined as the normalized magnitude of the NP density gradient $\sigma(\mathbf{r}) = \frac{|\nabla\Gamma(\mathbf{r})|}{\int d\mathbf{r}\,|\nabla\Gamma(\mathbf{r})|}$ and represents the distribution of grafting sites on the NPs.

By applying the Hubbard−Stratonovich transformation,[52] the following hybrid partition function is obtained

$$\mathcal{Z} = z_0 \int \mathcal{D}\{\omega\} \int d\mathbf{r}^{n_P}\, e^{-\mathcal{H}[\{\omega\}]} \tag{2}$$

where z_0 accounts for miscellaneous proportionality factors and $\{\omega\}$ represents a collection of different field terms and n_P is the number of explicit nanoparticles. The effective Hamiltonian ($\mathcal{H}$) provides access to free energy differences under the mean-field approximation; the difference between two effective Hamiltonians is equivalent to the change in free energy. The specific Hamiltonian for this system is derived as

$$\begin{aligned}\mathcal{H}[w_+,\ w_{AB}^{(\pm)},\ w_{AC}^{(\pm)},\ w_{BC}^{(\pm)}] &= \frac{\rho_0}{2\kappa}\int d\mathbf{r}\, w_+(\mathbf{r})^2 - i\int d\mathbf{r}\, w_+(\rho_0 - \check{\rho}_{NP}) \\ &+ \frac{\rho_0}{\chi_{AB}}\int d\mathbf{r}(w_{AB}^{(+)}(\mathbf{r})^2 + w_{AB}^{(-)}(\mathbf{r})^2) \\ &+ \frac{\rho_0}{\chi_{AC}}\int d\mathbf{r}(w_{AC}^{(+)}(\mathbf{r})^2 + w_{AC}^{(-)}(\mathbf{r})^2) + \frac{\rho_0}{-\chi_{BC}} \\ &\int d\mathbf{r}(w_{BC}^{(+)}(\mathbf{r})^2 + w_{BC}^{(-)}(\mathbf{r})^2) - n_D \log Q_D \\ &- n_{PEG}\int d\mathbf{r}\,\sigma_{PEG}(\mathbf{r})\ln(q_{PEG}(\mathbf{r}))\end{aligned} \tag{3}$$

where w_+ is the field enforcing the Helfand compressibility potential that discourages deviations from ρ_0, while κ is proportional to the incompressibility of the system; $\kappa = \infty$ corresponds to the incompressible limit. $\check{\rho}_{NP}$ is the microscopic density of the NPs convolved with the density function of the particles, $\check{\rho} = \sum_i^{N_P}(\delta * \Gamma)(\mathbf{r})$ where * represents a convolution of the two functions. The $\omega_{\alpha\beta}^{\pm}$ terms together represent the field conjugate to the Flory−Huggins interaction between species α and β, where $\alpha,\beta \in \{A, B, C\}$.[45] The number of BCP chains is denoted by n_D, and their partition function is represented as Q_D. Likewise, the partition function of the grafted chain is q_{PEG} and the number of grafted PEG brushes is n_{PEG}. The specific forms of Q_D and q_{PEG} and the various density operators can be found in the monograph by Fredrickson[52] as model E and model K and in other previous works.[21,37,45−50] The negative value of χ_{BC} accounts for the slightly negative χ between PMMA and PEG, χ_{AB} represents the repulsive interactions between PS and PMMA, and χ_{AC} between PS and PEG. The mean-field configurations are found using

DOI: 10.1021/acs.macromol.9b01324
Macromolecules 2019, 52, 8989−8999

a first-order semi-implicit relaxation scheme.[52] The inclusion of a negative χ requires a slightly different gradient scheme than that of Koski et al.[45] and follows the approach of Hore et al.;[51] complete details can be found in the Supporting Information.

Numerical Parameters. We approximate the experimental system, which has M_n = 38k-*b*-36.8k g/mol, as a discrete Gaussian chain A−B diblock copolymer with a composition (f_A) of 0.5 and a simulated molecular weight of M_n = 38k-*b*-36.625k g/mol. The data presented by Eitouni and Balsara[53] were then used to determine the statistical equivalent number of monomers and statistical segment size, which was then used to calculate R_g^2. To obtain the necessary values for the calculations (molar, statistical segment length, and number of monomers per statistical segment), the weighted average between the physical properties (monomer volume and statistical segment length) of the PS block and PMMA block was taken; for the presented system, the weighted average is a simple average since $\phi_{PS} = \phi_{PS} = 0.50$. Each block of the BCP is constituted of 30 beads with each statistical bead length (defined as 1*b* unit) representing 1.2332 nm; the statistical segment sizes for both blocks of the BCP are assumed to be the same. Therefore, one bead corresponds to roughly 12 monomeric units of the BCP. By maintaining the same statistical segment size for the grafted chain, each grafted simulation bead represents about 14 monomeric units of PEG.

Our simulations are performed in 2D, and, as a result, the rhombic nanoplates were modeled as 2D rods (which is analogous to looking at thin plates edge-on); the third dimension is assumed to be uniform, so this model corresponds to plates of infinite width. The thicknesses of the simulated plates (correspondingly, the diameter of the 2D rod) were 1.2918*b* units to match the 3 nm experimental size. The "diameter" of the simulated NPs (length of the 2D rod) is the average of the two unique experimental diagonals (d_1 and d_2) and is 6.1318*b*. The interface width of the NP ξ was chosen to be 0.2*b* units. The dimensionality of the 0.62 chains/nm^2 grafting density was reduced following the procedure established by Ferrier et al.[48] and then converted it to *b* units to obtain a grafting density of 1.43 chains/*b*. The χ values were also mapped from the experiments using the data collected by Eitouni and Balsara[53] and are as follows: $\chi_{PS/PMMA}$ = 0.501609, $\chi_{PS/PEG}$ = 1.13437, and $\chi_{PEG/PMMA}$ = −0.018209 using a reference volume of 0.1 nm^3. In combination with the χ values defined by Eitouni and Balsara,[53] a degree of polymerization (N) of 60 for the BCP was used to calculate $\chi_{AB}N$, while an N of 9 for the grafted brush was used to calculate both χ_{BC} and χ_{AC}. A κ of 50 was used in our simulations since the system equilibrates more easily at this value than a truly incompressible system ($\kappa = \infty$) while having negligible effects on the final results. In the 2D simulations, $\phi_x(\mathbf{r}) = \rho_x(\mathbf{r})/\rho_0$ where ϕ is the volume fraction of component x (PS, PMMA, PEG, or NP) with density ρ_x at position $\mathbf{r}$.

For the potential of mean force (PMF) simulations, the box size was 52.0*b* × 90.0*b* units with 525 × 875 collocation points, respectively, to contain four lamellar periods, and the SCFT equations were implemented and solved using pseudo-spectral techniques.[52] The angle rotation data was generated in a box with 65.0*b* × 70.0*b* units with 625 × 675 grid points, respectively, and contained five lamellar periods to minimize the amount of disturbance felt by the farthest BCP interface in the simulation. Unless noted, the NP dimensions, grafting density, χ, composition, and κ were all held constant. For discussion, the experimental equivalent of the simulation units will be used for the ease of the reader and authors.

Potential of Mean Force Curves. The PMF curves were generated with the aforementioned model and numerical parameters. The interparticle distance was varied between two explicit NPs at fractional distances of the box height, from 0.14 to 0.45. The farthest distance between simulated plates was used as the reference point to ensure that there are no interactions between the NPs. A separate set of simulations rotated a single explicit NP to generate the angle-dependent PMF curves from 0° to 10° in increments of 1° and higher angles of 20°, 30°, 45°, and 90°. No angle higher than 90° was probed due to symmetry. The 0° calculation was the reference state since this configuration minimizes the distortion to the BCP interface. Certain effects cannot be properly captured (such as NP tilt out-of-plane in the *z*-direction) since the simulations are 2D and not three-dimensional (3D).

RESULTS

The formation of ordered BCP nanocomposite films, containing nanoplates aligned with the lamellae and NP string assemblies, requires the surface modification of the as-synthesized, OA-stabilized GdF_3:Yb/Er nanoplates in Figure 1a. Consequently, OA was displaced by PEG-PO_3H_2 through a solution-phase ligand exchange. By establishing favorable interactions, the PEG-PO_3H_2-functionalized nanoplates in Figure 1b were incorporated and aligned in the PMMA domain of the parallel PS-*b*-PMMA lamellae in Figure 1c. We previously showed that these aligned and ordered films were attainable at low NP loadings (redisplayed in Figure S1 and Figure S2 for ϕ = 0.0083 and ϕ = 0.017, respectively). The nanoplate alignment and lamellae ordering behavior, however, breaks down at higher volume fractions and was the subject of our first study.[22] Here, we will instead focus on the emergence of interparticle assemblies and the anticipated domain distortion as a result of significant polymer chain stretching around rigid GdF_3:Yb/Er nanoplates.

While nanoplate alignment is clearly shown at ϕ = 0.0083 and ϕ = 0.017, the domain bulge cannot be resolved in the TEM images. Since PMMA sustains degradation by electron beam irradiation, the PMMA domains appear lighter than the PS domains in TEM due to increased *Z*-contrast.[54−56] This beam damage, in combination with the natural undulations in the BCP lamellae, also prevents the expected distortion around the nanoplates from being detected. To try and circumvent the limitations, posed by TEM, in experimentally visualizing the domain bulge, we performed GISAXS experiments on the BCP nanocomposites with ϕ = 0, ϕ = 0.0083, ϕ = 0.017, ϕ = 0.027, ϕ = 0.038, ϕ = 0.050, and ϕ = 0.064 PEG-PO_3H_2-functionalized GdF_3:Yb/Er and obtained an average lamellar period (λ). For high loadings of ϕ = 0.038, ϕ = 0.050, and ϕ = 0.064, the lamellar scattering peak was not observed, as seen in the top image of Figure S3. The absence of this peak indicates an extremely poorly ordered or even disordered phase, i.e., one without well-defined lamellar layers. In the sample containing ϕ = 0.038 nanoplates, the weak scattering peak indicates a predominantly disordered lamellar matrix. These results agree with our previous electron microscopy observations.[22] However, as long as lamellar formation persisted after processing the films, λ could be determined from the scattering data, as shown in the bottom image of Figure S3. We present λ for the evaluated ordered BCP nanocomposite samples as a function of NP volume fraction in Figure 2. For the neat (ϕ = 0) BCP, λ = 36.7 ± 0.2 nm. For the PS-*b*-PMMA lamellae with ϕ = 0.0083, ϕ = 0.017, and ϕ = 0.027 PEG-PO_3H_2-functionalized nanoplates, λ = 36.5 ± 0.5 nm, λ = 36.2 ± 0.2 nm, and λ = 35.9 ± 0.5 nm, respectively. Figure 2 and its inset show that there is no statistically significant difference in λ when nanoplates are incorporated into the PMMA domains, which could have confirmed that the predicted domain dilation had λ increased upon nanoplate insertion. We note that GISAXS provides an average measure of the structural order, and, thus, a given structural signal must be present in sufficient concentration to measurably shift a scattering peak. Given that the distortion introduced by the nanoplate is local and the concentration of the NPs is modest, it is not surprising that these local domain distortions do not measurably shift the GISAXS peak position.

DOI: 10.1021/acs.macromol.9b01324
Macromolecules 2019, 52, 8989−8999

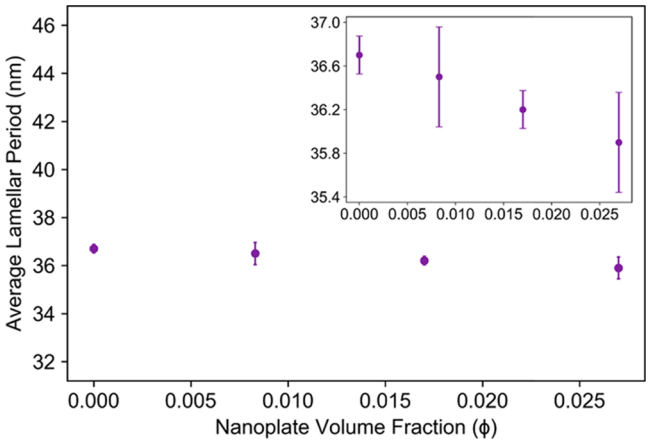

Figure 2. Average lamellar period (λ), experimentally determined from GISAXS, of ordered BCP nanocomposite films with $\phi = 0$, $\phi = 0.0083$, and $\phi = 0.017$ PEG-PO_3H_2-functionalized GdF_3:Yb/Er (20/2 mol %) and of a partially ordered sample with $\phi = 0.027$ nanoplates. The inset portrays the data with a narrower y-axis range. Error bars correspond to one standard deviation for three measurements collected in different locations on each sample.

While TEM and GISAXS are unable to experimentally corroborate the creation of a bulge around the GdF_3:Yb/Er nanoplates in the PMMA domains, as forecasted by Bockstaller et al.,[6] there is evidence in the TEM results, which suggests that the nanocomposite system finds a means to decrease the entropic cost attributed to expanding the PS/PMMA interface. By way of stringing nanoplates together in anisotropic arrays, the additional interfacial area from local domain distortions would decrease. This process of consolidating PS/PMMA interface is represented by the illustration shown in Figure S5. Merging at least two plates in a string would decrease the total amount of the PS/PMMA interface added to the system. Examples of these prevalent string assemblies for the ordered BCP film with $\phi = 0.017$ aligned GdF_3:Yb/Er are shown in Figure 3. The featured regions in Figure 3 showcase nanoplates coupled in strings of two, three, and up to six NPs in a row.

To understand the origin of the anisotropic NP assemblies, the PMF curve shown in Figure 4 was calculated to represent the free energy of two PEG-grafted nanoplates at fixed edge-to-edge separations (0.8 nm to 67.6 nm) while constrained to the center of the PMMA domain in a M_n = 38k-*b*-36.5k g/mol PS-*b*-PMMA lamellar diblock copolymer. A few notable features emerge in the PMF curve including a free energy maximum at a NP separation of 0.8 nm, a global minimum at 7.0 nm, a local

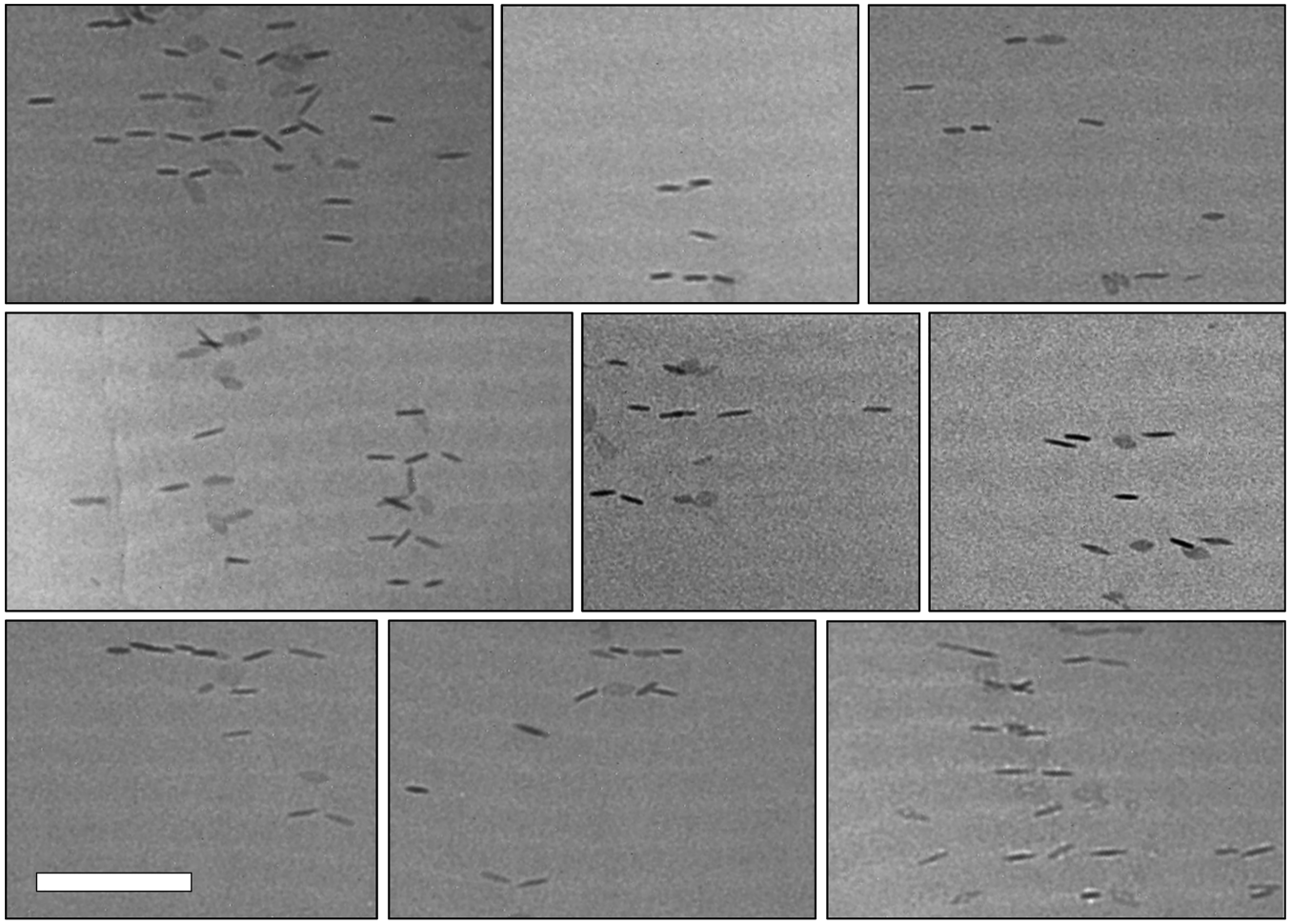

Figure 3. Representative TEM (JEM-1400, 120 kV) images of regions in annealed (190 °C, 48 h) and ultramicrotomed lamellar-forming M_n = 38k-*b*-36.8k g/mol PS-*b*-PMMA film cross-sections with $\phi = 0.017$ M_n = 5 kg/mol PEG-PO_3H_2-functionalized GdF_3:Yb/Er (20/2 mol %) highlighting nanoplates bridging together in strings. The light and dark domains of the BCP are PMMA and PS, respectively. Here, the imaging conditions are optimized to clearly visualize the nanoplate assemblies, sacrificing optimum contrast between PMMA and PS domains. The scale bar is 100 nm.

DOI: 10.1021/acs.macromol.9b01324
Macromolecules 2019, 52, 8989−8999

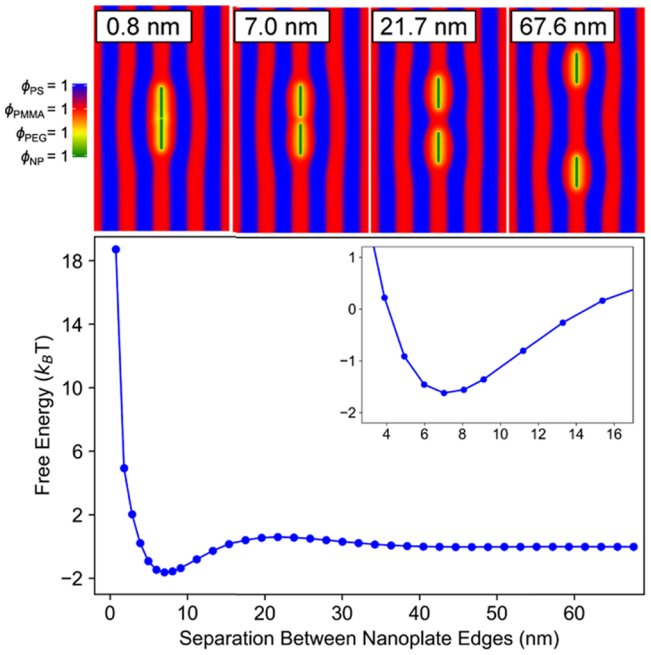

Figure 4. Potential of mean force curve to describe free energy as a function of edge-to-edge separation for two PEG-grafted nanoplates in the PMMA domain of PS-*b*-PMMA lamellae. The inset expands the region near the free energy minimum. (Top) 2D simulations show system representations at nanoplate separations of 0.8 nm, 7.0 nm, 21.7 nm, and 67.6 nm. PS, PMMA, PEG, and NP-rich regions are displayed as blue, red, yellow, and green, respectively.

maximum or activated state at 21.7 nm, and a plateau around 67.6 nm. The significance of these points can be explained by examining the BCP morphologies at these specific interparticle spacings. The 2D simulations in Figure 4 portray the morphological evolution of the system at the four points of interest for nanoplate separation. Importantly, at any of the depicted NP edge-to-edge distances, a bulge is observed around the nanoplates resulting in an increase of the unfavorable PS/PMMA interface. The bulge propagates to nearest neighbor domains, analogous to dislocations where the energy penalty adversely affects a few adjacent planes. While the maximum at 0.8 nm can best be characterized as hard NP overlap, the plateau occurring at the furthest most point corresponds to a region where particle−particle interactions start to become insignificant as the nanoplates are semi-infinitely spaced. The global minimum at 7.0 nm is associated with an equilibrium nanoplate separation originating from depletion−attraction interactions where this gap distance reflects the dimensions of unperturbed PEG brushes on both nanoplate surfaces. As shown in Figure 4 (top), the domain distortions around two approaching nanoplates combine into one bulge, thereby decreasing the total PS/PMMA area and minimizing the stretching and compression of the BCP and PEG chains. The free energy well centered around the minimum at an interparticle spacing of 7.0 nm is presented in the inset of Figure 4. The energy barrier identified at an intermediate NP separation of 21.7 nm seems to occur when the greatest degree of curvature in the interface is observed in Figure 4 (top). The source of this activated state will be explored further in our discussion.

To correlate the simulations to experiments and determine an experimental equilibrium interparticle spacing, 300 distances between nanoplate edges were measured from TEM images. All 300 measurements are shown in Table S1 and recast as a histogram exhibited in the top image of Figure 5

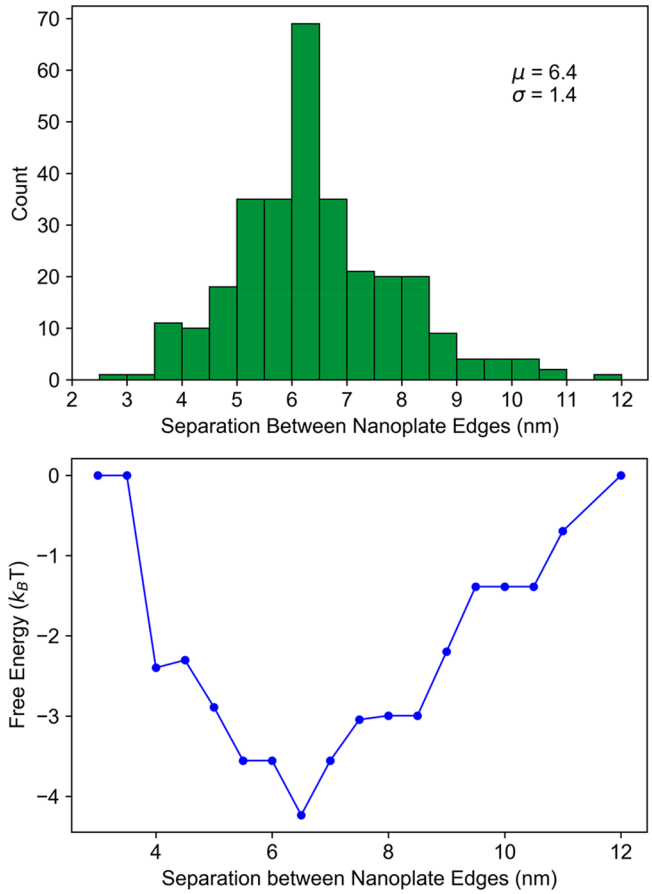

Figure 5. (Top) Histogram of experimentally measured separations between edges of PEG-PO_3H_2-functionalized nanoplates that are aligned in the PMMA domain of lamellar-forming PS-*b*-PMMA films. Nanoplates are bridging together in strings at a mean interparticle spacing (μ) of 6.4 nm with a standard deviation (σ) of 1.44 nm. (Bottom) Experimental free energy as a function of nanoplate edge-to-edge separation calculated by normalizing results in (top) over the total number of data points (300) to relate probability to energy using a Boltzmann distribution. The bin size is 0.5 nm.

with a bin size of 0.5 nm. The mean nanoplate spacing is 6.4 nm with a standard deviation of 1.44 nm. To convert the data represented in the histogram to an experimental free energy, probability values were first calculated by normalizing the histogram results over the total number of measurements (300). The probability (P) of finding two plates with a given separation can be related to the exponential of the free energy (F) by assuming equilibrium statistics hold

$$\frac{F}{k_BT} = -\ln P - \frac{F_0}{k_BT} \tag{4}$$

where k_B is the Boltzmann constant, T is the temperature, and F_0 is an irrelevant constant shift in the free energy. The resulting experimental free energy as a function of the nanoplate edge-to-edge distance is reproduced in the bottom plot of Figure 5 and can be compared to the simulation data in Figure 4. The equilibrium interparticle spacings corresponding to the global minima established by the PMF calculations and experimental data are 7.0 nm and 6.4 nm, respectively. Not

DOI: 10.1021/acs.macromol.9b01324
Macromolecules 2019, 52, 8989−8999

only are these strikingly similar separation values, but there is an excellent agreement between the asymmetric shape of the curves where the slope is steeper to the left and shallower to the right of the minimum. Therefore, simulations and experiments together suggest that nanoplate string formation occurs at interparticle spacings prescribed by the lowest-energy states in the well. The anisotropic assemblies emerge to avoid penalties posed by the energy barriers associated with (1) closely approaching the nanoplates to where the PEG chains would be severely compressed and NP overlap would occur and (2) isolating the GdF_3:Yb/Er particles at intermediate distances (~21.7 nm) where the highest curvature in the PS/PMMA interface is formed from adjoining domain bulges. Changes in interfacial area as a function of edge-to-edge nanoplate separation can be explored by defining the proxy for interfacial area $[A(\mathbf{r}_{NP})]$ as the average product of the PS and PMMA volume fractions over all positions in a given simulation box, $A(\mathbf{r}_{NP}) = \langle \int d\mathbf{r}\, \phi_{PS}(\mathbf{r})\phi_{PMMA}(\mathbf{r})\rangle_{\mathbf{r}}$. As shown in Figure 6, the interfacial area curve has a similar shape to the

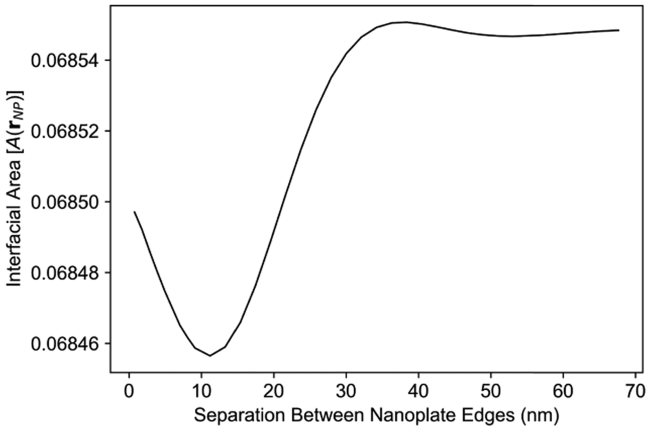

Figure 6. Interfacial area $[A(\mathbf{r}_{NP})]$ as a function of edge-to-edge separation for two PEG-grafted nanoplates in the PMMA domain of PS-*b*-PMMA lamellae.

free energy curve from Figure 4. However, the location of the $A(\mathbf{r}_{NP})$ minimum (11.2 nm) and maximum (38.4 nm) are offset from the free energy minimum (7.0 nm) and local maximum (21.7 nm). This indicates that while the interfacial area does contribute to the free energy extrema, it is not the sole contributor, which further supports the contribution of additional factors such as curvature in the PS/PMMA interface and conformational entropy penalties.

Another noticeable characteristic of the GdF_3:Yb/Er nanoplate alignment behavior is shown in Figure 3. Both the nanoplates assembled in strings and the nanoplates at far enough separation distances to remain isolated appear either well aligned or only slightly tilted in the PMMA domains. To understand the tolerance for nanoplate orientation in confined lamellar PS-*b*-PMMA domains, the PMF curve in Figure 7 was calculated to represent the free energy of one PEG-grafted nanoplate as a function of $\sin(\theta)$ where θ represents fixed orientations (0° to 90°) of the nanoplate constrained to the center of the PMMA domain in a M_n = 38k-*b*-36.5k g/mol PS-*b*-PMMA lamellar diblock copolymer. Here, confinement indicates that the domain spacing of the nearly symmetric BCP is smaller than the longest and shortest diagonal of the rhombic nanoplate but larger than the nanoplate thickness. At low nanoplate tilts (0° to 10°), the change in free energy is

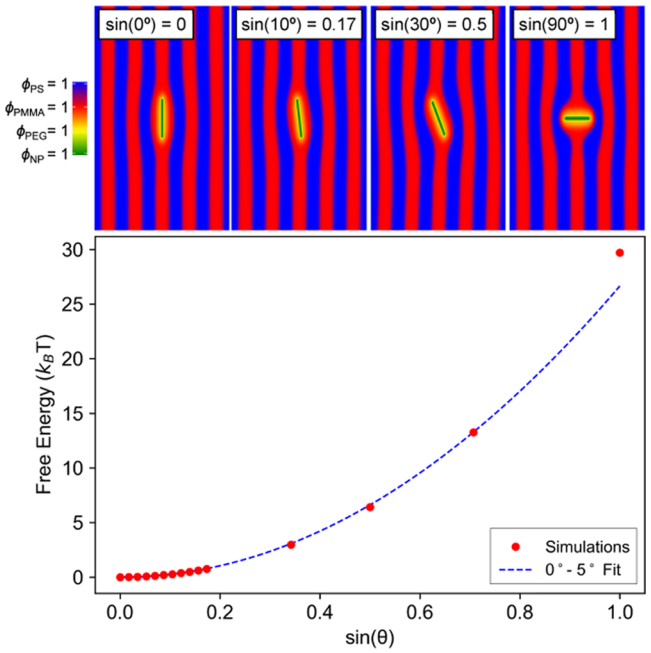

Figure 7. Potential of mean force curve to describe free energy (red) as a function of $\sin(\theta)$ where θ is the orientation of one PEG-grafted nanoplate in the PMMA domain of PS-*b*-PMMA lamellae. A quadratic regression (blue) was performed from sin(0°) to sin(5°). (Top) 2D simulations at nanoplate orientations of 0°, 10°, 30°, and 90°. PS, PMMA, PEG, and NP-rich regions are displayed as blue, red, yellow, and green, respectively.

relatively small compared to high orientation angles. By considering the BCP morphologies in the 2D simulations of Figure 7, the domain distortion and, thus, the PS/PMMA interface are shown to increase substantially as the nanoplate is tilted from 0° to 10° to 30° and to 90°. Neighboring domains are also more significantly perturbed at higher nanoplate orientation angles. Interestingly, when the PMF data is fit with a quadratic regression performed over $\sin(0°)$ to $\sin(5°)$ (shown in Figure 7), the fit curve correctly estimates the energy cost of high angles. This agreement will be further investigated in our discussion. The simulations, however, verify that GdF_3:Yb/Er nanoplates are able to assume a range of low tilt angles in the PMMA domain of the nanocomposite films because the energy penalties are relatively small, <1 k_BT.

DISCUSSION

We will first consider the origin of the free energy reduction, demonstrated in the PMF curve of Figure 4, as two nanoplates are moved from a separation distance of 21.7 nm to 7.0 nm, which corresponds to the locations of the energy barrier and the equilibrium interparticle spacing, respectively. Listak and Bockstaller previously showed that PS-functionalized spherical NPs dispersed in nearly symmetric bulk lamellar-forming poly(styrene-*b*-ethylene propylene) (PS-*b*-PEP) localize at high-energy defects like high tilt (omega-type) and T-junction grain boundaries.[57] By redistributing NPs to these unfavorable lamellar structures, the authors elucidate a mechanism where NPs accumulate to stabilize the grain boundaries. More specifically, energetic costs related to perturbing the equilibrium BCP morphology are diminished by swelling these junctions with NPs. NP segregation alleviates the conformational energy penalties of highly stretched BCP chains imposed

DOI: 10.1021/acs.macromol.9b01324
Macromolecules 2019, 52, 8989−8999

by forming the omega-type and T-junction defects. The T-junctions, in particular, not only contain exceptionally curved PS/PEP interfaces but also produce more interfacial area than the equilibrium microstructure. As a result, Listak and Bockstaller observed "3D 'stringlike' particle aggregates" along these structures. Experiments by Rasin et al. also show that poly(2-vinylpyridine) (P2VP)-grafted gold nanorods dispersed in cylindrical-forming PS-*b*-P2VP collect at the base of vertical P2VP cylinders.[21] The nanorods relieve local chain stretching caused by the minority P2VP domain wetting the substrate in a T-junction-like defect. Subsequent simulations from Koski et al. show that as the tilt angle of omega-type like defects in a BCP decreases (therefore, the curvature of A/B interface increases), NP accumulation becomes more prominent as a result of a greater extent of chain stretching.[58]

In the present system, intermediate separations (21.7 nm) of aligned PEG-PO_3H_2-grafted GdF_3:Yb/Er nanoplates promote the greatest distortion in the equilibrium BCP morphology. At these edge-to-edge nanoplate distances, the added PS/PMMA interfacial area formed from the domain bulges converges to create a region of the PS/PMMA interface with the greatest possible curvature. This high-energy state corresponds to the energy barrier seen as a local maximum in the simulation results in Figure 4. Therefore, at a predicted separation of 21.7 nm between nanoplate edges, the conformational entropy penalty associated with chains from both the PS and PMMA blocks stretching to fill the space created by the defect is presumed to be the greatest. Therefore, bridging PEG-PO_3H_2-functionalized nanoplates into string assemblies not only decreases the degree of chain stretching but also decreases the interfacial area between the PS and PMMA microdomains. The nanoplates are, in essence, attracted to each other to create anisotropic assemblies with interparticle spacings prescribed by the energy well shown in simulations (Figure 4) and corroborated by experiments (Figure 5). Ultimately, the gain in free energy associated with decreasing interfacial area and minimizing chain stretching must be outweighed by the energy penalty associated with reducing the translational entropy associated with evenly distributing GdF_3:Yb/Er nanoplates. Both the simulations and the emergence of anisotropic PEG-PO_3H_2-functionalized GdF_3:Yb/Er nanoplate assemblies aligned in the PMMA domain of M_n = 38k-*b*-36.5k g/mol PS-*b*-PMMA shown experimentally in Figure 3 indicate that this energetic criterion is fulfilled.

In the experimental BCP nanocomposites films containing ϕ = 0.0083 and ϕ = 0.017 PEG-grafted GdF_3:Yb/Er nanoplates, the NPs are highly oriented in the ordered parallel lamellae. The free energy calculations in Figure 7 support the alignment of nanoplates confined in the PMMA domain at low orientation angles since the free energy increases considerably beyond ~10°. Pryamitsyn and Ganesan present analogies that have been made between polymer brushes grafted onto flat substrates and the A and B polymers of an A−B lamellar-forming BCP (illustrated in Figure S6a and Figure S6b).[59] Based on prior results, the authors express the pressure field [$P(z)$ in k_BT units] on a polymer brush with height h at a position z from the substrate as[59]

$$P(z) \sim \left(1 - \frac{z^2}{h^2}\right) \tag{5}$$

When a spherical NP is placed within the brush layer, the change in free energy, $dF_{brush}(z)$, is proportional to the pressure at a given point in the brush multiplied by the differential volume element of the NP (dV_{NP}), shown in Figure S6c and as[59]

$$dF_{brush}(z) \sim -P(z)\, dV_{NP} \tag{6}$$

We can then generalize this model, describing spherical NPs, to our nanoplates by considering a differential volume element of the nanoplate at distance x along a nanoplate that is rotated θ (schematic in Figure S6d). The change in free energy for nanoplates place within the brush layer can then be recast as[59]

$$dF_{brush}(\theta) \sim -\left(1 - \frac{(h - x\sin\theta)^2}{h^2}\right) dV_{NP} \tag{7}$$

Consistent with this expression, the simulation results in Figure 7 are shown to fit a quadratic regression with respect to $\sin(\theta)$ even when performed from only over $\sin(0°)$ to $\sin(5°)$. However, and importantly, Pryamitsyn and Ganesan note that $dF_{brush}(z)$ only applies when the distortions, attributed to inserting a NP in the center of the domain, are relatively small.[59] We would, therefore, expect the quadratic approximation breaks down at higher tilt angles. Equation 6 not only assumes that the perturbations are small but also assumes that the substrate is fixed. A key difference in the present system is that our "substrate" (the PS/PMMA interface) can move, and, therefore, the dynamic behavior of the A/B BCP interface distorting around the NP helps to restore chains from highly compressed states. Therefore, because small perturbations are maintained as defined by Pryamitsyn and Ganesan, we would expect the regression to overestimate the PMF curve. However, since the simulated results in Figure 7 do not deviate from the quadratic regression, additional energy terms, like the previously discussed interfacial area and curvature, must exist. Ultimately, we credit the strong alignment of nanoplates in lamellar-forming M_n = 38k-*b*-36.8k g/mol PS-*b*-PMMA film to limit the entropic cost attributed to large chain deformations. This conclusion is also supported by previous results from Deshmukh et al. where a narrow tolerance of orientation angles ($-5° \leq \theta \leq 5°$) was observed in 71% of PEG-thiol-functionalized gold nanorods aligned in PS-*b*-PMMA lamellae.[19]

CONCLUSIONS

The formation of anisotropic string assemblies and the anticipated domain bulge around M_n = 5 kg/mol PEG-PO_3H_2-functionalized GdF_3:Yb/Er (20/2 mol %) nanoplates aligned in parallel lamellar-forming M_n = 38k-*b*-36.8k g/mol PS-*b*-PMMA films was investigated. Although electron microscopy and scattering techniques were unable to experimentally probe the local domain distortion, nanoplate strings with a mean interparticle spacing of 6.4 nm were observed. Complementary hSCFT simulations mapped the pairwise interactions between two PEG-grafted nanoplates aligned in the PMMA domain. The 2D simulations not only show the morphological effects of nanoplate insertion, clearly depicting the local domain distortion, but also predict an equilibrium interparticle spacing of 7.0 nm that is in good agreement with experiments. The free energy well, centered around the free energy minima, of the calculated PMF curves is corroborated by the experiments where the edge-to-edge distances in nanoplate strings range from ~2.5 nm to ~12 nm.

DOI: 10.1021/acs.macromol.9b01324
Macromolecules 2019, 52, 8989−8999

The emergence of anisotropic nanoplate assemblies within this span of interparticle spacings is consistent with minimizing the effects of (1) excessive PEG chain compression at small separations and (2) forming regions of high curvature in the PS/PMMA interface accompanied by large conformational entropy costs at intermediate separations. Additional simulations show <1 k_BT changes in free energy at low tilt orientations of nanoplates, which supports the high degree of alignment observed experimentally. Harnessing the shape-dependent properties of nanoplates and not only directing their orientation but also controlling their interparticle spacing in a polymer matrix is particularly attractive for a variety of applications, including plasmonic coupling. To further tune the edge-to-edge separation of nanoplates in a BCP film, the effect of BCP and grafted chain molecular weights on the shape of the PMF curves, the location of important features, and, consequently, the formation of string assemblies will be the subject of a future publication. Ultimately, the simulation framework presented within can be leveraged to understand how unexplored parameters such as grafting density, χ, and BCP morphology affect the overall phase behavior of BCP nanocomposites containing nanoplates.

■ ASSOCIATED CONTENT

Supporting Information

The Supporting Information is available free of charge on the ACS Publications website at DOI: 10.1021/acs.macromol.9b01324.

BCP-based PNCs with ϕ = 0.0083 and ϕ = 0.017 PEG-PO_3H_2-functionalized GdF_3:Yb/Er (20/2 mol %), typical peak analyses from GISAXS, the ImageJ process to ascertain edge-to-edge nanoplate separations, table of the 300 measured NP separation values, and an illustration of nanoplates merging together to consolidate the PS/PMMA interface (PDF)

■ AUTHOR INFORMATION

Corresponding Authors

*E-mail: cbmurray@sas.upenn.edu (C.B.M.).
*E-mail: rrig@seas.upenn.edu (R.A.R.).
*E-mail: composto@seas.upenn.edu (R.J.C.).

ORCID

Nadia M. Krook: 0000-0003-3308-9040
Kevin G. Yager: 0000-0001-7745-2513
Robert A. Riggleman: 0000-0002-5434-4787
Russell J. Composto: 0000-0002-5906-2594

Author Contributions

⊥N.M.K. (experiments) and C.T. (simulations) contributed equally to this work.

Notes

The authors declare no competing financial interest.

■ ACKNOWLEDGMENTS

We acknowledge funding from the National Science Foundation with support from the POLYMERS-DMR-1507713 and 1905912 (N.M.K., R.J.C.), PIRE-OISE-1545884 (N.M.K., C.T., C.B.M., R.A.R., R.J.C.), and MRSEC-DMR-1720530 (N.M.K., C.B.M., R.J.C.) programs as well as partial support from ANR-15-PIRE-0001-07. K.C.E. acknowledges support from the NSF Graduate Research Fellowship Program under Grant No. DGE-1321851. The authors also gratefully acknowledge the computational resources provided by XSEDE facilities through award TG-DMR-150034. This research used resources of the Center for Functional Nanomaterials and the National Synchrotron Light Source II, which are U.S. DOE Office of Science Facilities, at Brookhaven National Laboratory under Contract No. DE-SC0012704. The authors acknowledge Dr. Karen I. Winey for use of the vacuum furnaces and ultramicrotome in her laboratory. We are also grateful for the helpful discussions with Michael J. Boyle, Boris Rasin, and Benjamin J. Lindsay.

■ REFERENCES

(1) Zhao, Y.; Thorkelsson, K.; Mastroianni, A. J.; Schilling, T.; Luther, J. M.; Rancatore, B. J.; Matsunaga, K.; Jinnai, H.; Wu, Y.; Poulsen, D.; Fréchet, J. M. J.; Alivisatos, A. P.; Xu, T. Small-Molecule-Directed Nanoparticle Assembly Towards Stimuli-Responsive Nanocomposites. *Nat. Mater.* **2009**, *8*, 979−985.

(2) Thorkelsson, K.; Mastroianni, A. J.; Ercius, P.; Xu, T. Direct Nanorod Assembly Using Block Copolymer-Based Supramolecules. *Nano Lett.* **2012**, *12*, 498−504.

(3) Li, W.; Zhang, P.; Dai, M.; He, J.; Babu, T.; Xu, Y.-L.; Deng, R.; Liang, R.; Lu, M.-H.; Nie, Z.; Zhu, J. Ordering of Gold Nanorods in Confined Spaces by Directed Assembly. *Macromolecules* **2013**, *46*, 2241−2248.

(4) Thorkelsson, K.; Nelson, J. H.; Alivisatos, A. P.; Xu, T. End-to-End Alignment of Nanorods in Thin Films. *Nano Lett.* **2013**, *13*, 4908−4913.

(5) Hsu, S.-W.; Xu, T. Tailoring Co-assembly of Nanodiscs and Block Copolymer-Based Supramolecules by Manipulating Interparticle Interactions. *Macromolecules.* **2019**, *52*, 2833−2842.

(6) Bockstaller, M. R.; Mickiewicz, R. A.; Thomas, E. L. Block Copolymer Nanocomposites: Perspectives for Tailored Functional Materials. *Adv. Mater.* **2005**, *17*, 1331−1349.

(7) Hoheisel, T. N.; Hur, K.; Wiesner, U. B. Block Copolymer-Nanoparticle Hybrid Self-Assembly. *Prog. Polym. Sci.* **2015**, *40*, 3−32.

(8) Sarkar, B.; Alexandridis, P. Block Copolymer-Nanoparticle Composites: Structure, Functional Properties, and Processing. *Prog. Polym. Sci.* **2015**, *40*, 33−62.

(9) Thompson, R. B.; Ginzburg, V. V.; Matsen, M. W.; Balazs, A. C. Predicting the Mesophases of Copolymer-Nanoparticle Composites. *Science* **2001**, *292*, 2469−2472.

(10) Thompson, R. B.; Ginzburg, V. V.; Matsen, M. W.; Balazs, A. C. Block Copolymer-Directed Assembly of Nanoparticles: Forming Mesoscopically Ordered Hybrid Materials. *Macromolecules* **2002**, *35*, 1060−1071.

(11) Bockstaller, M. R.; Lapetnikov, Y.; Marge, S.; Thomas, E. L. Size-Selective Organization of Enthalpic Compatibilized Nanocrystals in Ternary Block Copolymer/Particle Mixtures. *J. Am. Chem. Soc.* **2003**, *125*, 5276−5277.

(12) Lin, Y.; Böker, A.; He, J.; Sill, K.; Xiang, H.; Abetz, C.; Li, X.; Wang, J.; Emrick, T.; Long, S.; Wang, Q.; Balazs, A.; Russell, T. P. Self-Directed Self-Assembly of Nanoparticle/Copolymer Mixtures. *Nature* **2005**, *434*, 55−59.

(13) Chiu, J. J.; Kim, B. J.; Kramer, E. J.; Pine, D. J. Control of Nanoparticle Location in Block Copolymers. *J. Am. Chem. Soc.* **2005**, *127*, 5036−5037.

(14) Balazs, A. C.; Emrick, T.; Russell, T. P. Nanoparticle Polymer Composites: Where Two Small Worlds Meet. *Science* **2006**, *314*, 1107−1110.

(15) Kim, B. J.; Bang, J.; Hawker, C. J.; Kramer, E. J. Effect of Areal Chain Density on the Location of Polymer-Modified Gold Nanoparticles in a Block Copolymer Template. *Macromolecules* **2006**, *39*, 4108−4114.

(16) Chiu, J. J.; Kim, B. J.; Yi, G.; Band, J.; Kramer, E. J.; Pine, D. J. Distribution of Nanoparticles in Lamellar Domains of Block Copolymers. *Macromolecules* **2007**, *40*, 3361−3365.

(17) Kim, B. J.; Bang, J.; Hawker, C. J.; Chiu, J. J.; Pine, D. J.; Jang, S. G.; Yang, S.; Kramer, E. J. Creating Surfactant Nanoparticles for

DOI: 10.1021/acs.macromol.9b01324
Macromolecules 2019, 52, 8989−8999

Block Copolymer Composites through Surface Chemistry. *Langmuir* **2007**, *23*, 12693−12703.
(18) Kim, B. J.; Fredrickson, G. H.; Kramer, E. J. Effect of Polymer Ligand Molecular Weight on Polymer-Coated Nanoparticle Location in Block Copolymers. *Macromolecules* **2008**, *41*, 436−447.
(19) Deshmukh, R. D.; Liu, Y.; Composto, R. J. Two-Dimensional Confinement of Nanorods in Block Copolymer Domains. *Nano Lett.* **2007**, *7*, 3662−3668.
(20) Ploshnik, E.; Salant, A.; Banin, U.; Shenhar, R. Hierarchical Surface Patterns of Nanorods Obtained by Co-Assembly with Block Copolymers in Ultrathin Films. *Adv. Mater.* **2010**, *22*, 2774−2779.
(21) Rasin, B.; Chao, H.; Jiang, G.; Wang, D.; Riggleman, R. A.; Composto, R. J. Dispersion and Alignment of Nanorods in Cylindrical Block Copolymer Thin Films. *Soft Matter* **2016**, *12*, 2177−2185.
(22) Krook, N. M.; Ford, J.; Maréchal, M.; Rannou, P.; Meth, J. S.; Murray, C. B.; Composto, R. J. Alignment of Nanoplates in Lamellar Diblock Copolymer Domains and the Effect of Particle Volume Fraction on Phase Behavior. *ACS Macro Lett.* **2018**, *7*, 1400−1407.
(23) Zhang, S.; Pelligra, C. I.; Feng, X.; Osuji, C. O. Directed Assembly of Hybrid Nanomaterials and Nanocomposites. *Adv. Mater.* **2018**, *30*, No. 1705794.
(24) Zhang, S.; Pelligra, C. I.; Keskar, G.; Jiang, J.; Majewski, P. W.; Taylor, A. D.; Ismail-Beigi, S.; Pfefferle, L. D.; Osuji, C. O. Directed Self-Assembly of Hybrid Oxide/Polymer Core/Shell Nanowires with Transport Optimized Morphology for Photovoltaics. *Adv. Mater.* **2012**, *24*, 82−87.
(25) Pelligra, C. I.; Majewski, P. W.; Osuji, C. O. Large Area Vertical Alignment of ZnO Nanowires in Semiconducting Polymer Thin Films Directed by Magnetic Fields. *Nanoscale* **2013**, *5*, 10511−10517.
(26) Diroll, B. T.; Greybush, N. J.; Kagan, C. R.; Murray, C. B. Smetic Nanorod Superlattices Assembled on Liquid Subphases: Structure, Orientation, Defects, and Optical Polarization. *Chem. Mater.* **2015**, *27*, 2998−3008.
(27) Stebe, K. J.; Lewandowski, E.; Ghosh, M. Oriented Assembly of Metamaterials. *Science* **2009**, *325*, 159−160.
(28) Liu, Q.; Ackerman, P. J.; Lubensky, T. C.; Smalyukh, I. I. Biaxial Ferromagnetic Liquid Crystal Colloids. *Proc. Natl. Acad. Sci. U.S.A.* **2016**, *113*, 10479−10484.
(29) Liu, Z.; Xu, Z.; Hu, X.; Gao, C. Lyotropic Liquid Crystal of Polyacrylonitrile-Grafted Graphene Oxide and its Assembled Continuous Strong Nacre-Mimetic Fibers. *Macromolecules* **2013**, *46*, 6931−6941.
(30) Chen, J.; Huang, X.; Sun, B.; Wang, Y.; Zhu, Y.; Jiang, P. Vertically Aligned and Interconnected Boron Nitride Nanosheets for Advanced Flexible Nanocomposite Thermal Interface Materials. *ACS Appl. Mater. Interfaces* **2017**, *9*, 30909−30917.
(31) Akcora, P.; Liu, H.; Kumar, S. K.; Moll, J.; Li, Y.; Benicewicz, B. C.; Schadler, L. S.; Acehan, D.; Panagiotopoulos, A. Z.; Pryamitsyn, V.; Ganesan, V.; Ilavsky, J.; Thiyagarajan, P.; Colby, R. H.; Douglas, J. F. Anisotropic Self-Assembly of Spherical Polymer-Grafted Nanoparticles. *Nat. Mater.* **2009**, *8*, 354−359.
(32) Gao, B.; Arya, G.; Tao, A. R. Self-Orienting Nanocubes for the Assembly of Plasmonic Nanojunctions. *Nat. Nanotechnol.* **2012**, *7*, 433−437.
(33) Ferrier, R. C., Jr.; Lee, H.-S.; Hore, M. J. A.; Caporizzo, M.; Eckmann, D. M.; Composto, R. J. Gold Nanorod Linking to Control Plasmonic Properties in Solution and Polymer Nanocomposites. *Langmuir* **2014**, *30*, 1906−1914.
(34) Gurunatha, K. L.; Marvi, S.; Arya, G.; Tao, A. R. Computationally Guided Assembly of Oriented Nanocubes by Modulating Grafted Polymer-Surface Interactions. *Nano Lett.* **2015**, *15*, 7377−7382.
(35) Lee, J. Y.; Shou, Z.; Balazs, A. C. Predicting the Morphologies of Confined Copolymer/Nanoparticle Mixtures. *Macromolecules* **2003**, *36*, 7730−7739.
(36) Sides, S. W.; Kim, B. J.; Kramer, E. J.; Fredrickson, G. H. Hybrid Particle-Field Simulations of Polymer Nanocomposites. *Phys. Rev. Lett.* **2006**, *96*, No. 250601.
(37) Matsen, M. W.; Thompson, R. B. Particle Distributions in a Block Copolymer Nanocomposite. *Macromolecules* **2008**, *41*, 1853−1860.
(38) Hur, K.; Henning, R. G.; Escobedo, F. A.; Wiesner, U. Mesoscopic Structure Prediction of Nanoparticle Assembly and Coassembly: Theoretical Foundation. *J. Chem. Phys.* **2010**, *133*, No. 194108.
(39) Ting, C. L.; Composto, R. J.; Frischknecht, A. L. Orientational Control of Polymer Grafted Nanorods. *Macromolecules* **2016**, *49*, 1111−1119.
(40) Yoneda, Y. Anomalous Surface Reflection of X Rays. *Phys. Rev.* **1963**, *131*, 2010−2013.
(41) Sinha, S. K.; Sirota, E. B.; Garoff, S.; Stanley, H. B. X-ray and Neutron Scattering From Rough Surfaces. *Phys. Rev. B* **1988**, *38*, 2297−2311.
(42) Lee, B.; Park, I.; Yoon, J.; Park, S.; Kim, J.; Kim, K.-W.; Chang, T.; Ree, M. Structural Analysis of Block Copolymer Thin Films with Grazing Incidence Small-Angle X-ray Scattering. *Macromolecules* **2005**, *38*, 4311−4323.
(43) Lu, X.; Yager, K. G.; Johnston, D.; Black, C. T.; Ocko, B. M. Grazing-Incidence Transmission X-ray Scattering: Surface Scattering in the Born Approximation. *J. Appl. Crystallogr.* **2013**, *46*, 165−172.
(44) Liu, J.; Yager, K. G. Unwarping GISAXS Data. *IUCrJ* **2018**, *5*, 737−752.
(45) Koski, J.; Chao, H.; Riggleman, R. A. Field Theoretic Simulations of Polymer Nanocomposites. *J. Chem. Phys.* **2013**, *139*, No. 244911.
(46) Hickey, R. J.; Koski, J.; Meng, X.; Riggleman, R. A.; Zhang, P.; Park, S.-J. Size-Controlled Self-Assembly of Superparamagnetic Polymersomes. *ACS Nano* **2014**, *8*, 495−502.
(47) Koski, J.; Chao, H.; Riggleman, R. A. Predicting the Structure and Interfacial Activity of Diblock Brush, Mixed Brush, and Janus-Grafted Nanoparticles. *Chem. Commun.* **2015**, *51*, 5440−5443.
(48) Ferrier, R. C., Jr.; Koski, J.; Riggleman, R. A.; Composto, R. J. Engineering the Assembly of Gold Nanorods in Polymer Matrices. *Macromolecules* **2016**, *49*, 1002−1015.
(49) Koski, J. P.; Riggleman, R. A. Field-Theoretic Simulations of Block Copolymer Nanocomposites in a Constant Interfacial Tension Ensemble. *J. Chem. Phys.* **2017**, *146*, No. 164903.
(50) Chao, H.; Lindsay, B. J.; Riggleman, R. A. Field-Theoretic Simulations of the Distribution of Nanorods in Diblock Copolymer Thin Films. *J. Phys. Chem. B.* **2017**, *121*, 11198−11209.
(51) Hore, M. J. A.; Composto, R. J. Using Miscible Polymer Blends to Control Depletion-Attraction Forces Between Au Nanorods in Nanocomposite Films. *Macromolecules* **2012**, *45*, 6078−6086.
(52) Fredrickson, G. H. *The Equilibrium Theory of Inhomogeneous Polymers*; Oxford University Press, 2006.
(53) Eitouni, H. B.; Balsara, N. P. Thermodynamics of Polymer Blends. In *Physical Properties of Polymers Handbook*, 2nd ed.; Mark, J. E., Ed.; Springer: New York, 2007; Chapter 19, pp 339−356.
(54) Choi, J. O.; Moore, J. A.; Corelli, J. C.; Silverman, J. P.; Bakhru, H. Degradation of Poly(Methylmethacylate) by Deep Ultraviolet, X-ray, Electron Beam, and Proton Beam Irradiation. *J. Vac. Sci. Technol., B: Microelectron. Nanometer Struct.—Process., Meas., Phenom.* **1988**, *6*, 2286−2289.
(55) Tang, C.; Lennon, E. M.; Fredrickson, G. H.; Kramer, E. J.; Hawker, C. J. Evolution of Block Copolymer Lithography to Highly Ordered Square Arrays. *Science* **2008**, *322*, 429−432.
(56) Egerton, R. F. Mechanisms of Radiation Damage in Beam-Sensitive Specimens, for TEM Accelerating Voltages Between 10 and 300 kV. *Microsc. Res. Tech.* **2012**, *75*, 1550−1556.
(57) Listak, J.; Bockstaller, M. R. Stabilization of Grain Boundary Morphologies in Lamellar Block Copolymer/Nanoparticle Blends. *Macromolecules* **2006**, *39*, 5820−5825.
(58) Koski, J.; Hagberg, B.; Riggleman, R. A. Attraction of Nanoparticles in Tilt Grain Boundaries in Block Copolymers. *Macromol. Chem. Phys.* **2016**, *217*, 509−518.

DOI: 10.1021/acs.macromol.9b01324
Macromolecules 2019, 52, 8989−8999

(59) Pryamitsyn, V.; Ganesan, V. Strong Segregation Theory of Block Copolymer-Nanoparticle Composites. *Macromolecules* **2006**, *39*, 8499−8510.

DOI: 10.1021/acs.macromol.9b01324
Macromolecules 2019, 52, 8989−8999